

UCLA

UCLA Previously Published Works

Title

Yield Surface Mapping and Triaxial Compression Test Data Curation

Permalink

<https://escholarship.org/uc/item/19k2b28t>

Authors

Eslami, Mohammad M

Brandenberg, Scott J

Pradel, Daniel

et al.

Publication Date

2018

Peer reviewed

1 **Experimental Mapping of Elastoplastic Surfaces for Sand Using** 2 **Undrained Perturbations**

3 **by Mohammad M. Eslami¹, Daniel Pradel², and Scott J. Brandenburg³**

4 **Abstract**

5 Elastoplastic models are commonly used in modern geotechnical practice to numerically
6 predict displacements, stresses, and pore pressures in large construction projects. These
7 elastoplastic models use presumed functional forms for yield and plastic potential functions
8 that are rarely obtained from experimental measurements. This research describes a simple
9 experimental technique that can be used to obtain the slopes of the plastic potential and yield
10 functions during shear based on the deformation theory of plasticity. The method imposes small
11 perturbations in the direction of the stress increment by closing the drainage valve, thereby
12 abruptly switching from drained to undrained loading conditions during plastic loading.
13 Elastoplastic moduli are obtained immediately before and after the perturbation from the
14 measured deviatoric stress, mean effective stress, deviatoric strains, and volumetric strains for
15 the stress paths immediately before and immediately after closing the drain valve. During
16 drained shear, samples were sheared while the mean effective stress was maintained constant.
17 Combining tests performed at several confining stresses, the proposed method can map
18 conventional isotropic yield and plastic potential surfaces and predict their evolution for a wide
19 range of stresses. The proposed technique can also be used for kinematic yield surface and may
20 be used to develop new and more accurate elastoplastic constitutive models.

¹ 2270 Boelter Hall, Department of Civil and Environmental Engineering, University of California, Los Angeles, CA 90095-1593.

² Hitchcock Hall, 2070 Neil Avenue, Department of Civil, Environmental, and Geologic Engineering, Ohio State University, Columbus, OH 43210

³ 5731 Boelter Hall, Department of Civil and Environmental Engineering, University of California, Los Angeles, CA 90095-1593. Email: sjbrandenberg@ucla.edu. Corresponding author.

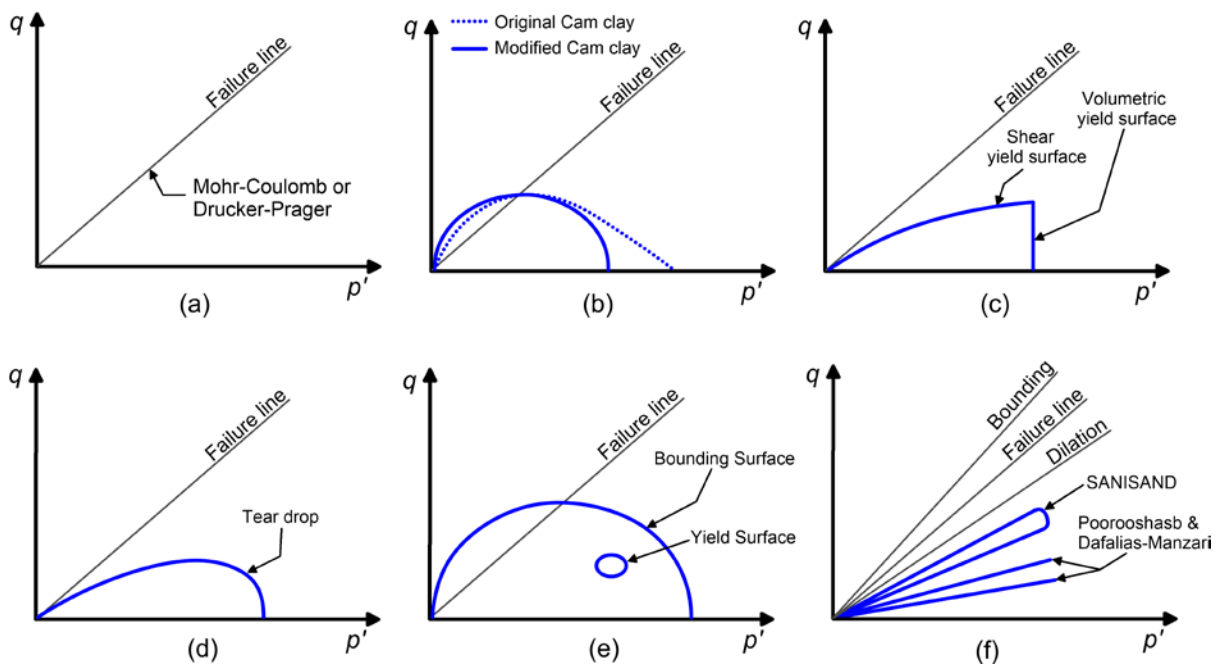
21 **Keywords: soil plasticity, yield surface, plastic potential, plastic flow, constitutive**
22 **modeling, non-associated flow, elastoplastic behavior.**

23 **Introduction**

24 Using numerical simulations to predict permanent deformations caused by surcharges,
25 excavations and other similar geotechnical loading mechanisms, requires constitutive models
26 that successfully estimate the anticipated level of irrecoverable strains. The use of numerical
27 modelling for the design of large geotechnical projects has become widespread in recent years,
28 especially for large infrastructure projects such as dams, tunnels, and highway embankments,
29 as well as for deep excavations next to existing buildings. The considerable importance of
30 modelling in the analysis and design of geo-structures was acknowledged in 2010, when it was
31 named one of the focus areas at the Geo-Institute's national conferences (ASCE, 2010).

32 Constitutive models commonly implemented in finite element computer programs, such as
33 PLAXIS (2015) or finite difference programs such as FLAC (Itasca, 2011) are generally
34 elastoplastic in nature and use single or dual isotropic yield surfaces. As illustrated in Fig. 1,
35 commonly used models exhibit significant differences in the treatment of yield surfaces and
36 plastic potential surfaces. The simplest models consist of a Mohr-Coulomb or Drucker-Prager
37 type yield surface, with the plastic flow direction controlled by a constant dilation angle (Fig.
38 1a). These models neglect many fundamental features of soil behavior, including plastic
39 volumetric flow under isotropic loading conditions (i.e., do not generate irrecoverable strains
40 in isotropic consolidation), small-strain yielding, and critical state soil mechanics. Roscoe and
41 Schofield (1963) introduced the original Cam-clay model (Fig. 1b), which utilizes a
42 logarithmic function to define the yield surface in the q - p' stress invariant space, and an
43 associated flow rule (i.e., the plastic potential surface and yield surface coincide). This model
44 conforms to critical state soil mechanics, meaning that the failure condition is associated with
45 zero volumetric strain rate as the plastic shear strains continue to accumulate, and it is capable

46 of capturing consolidation behavior though its yield surface generates deviatoric strains under
 47 isotropic consolidation conditions. The modified Cam-clay model (Roscoe and Burland, 1968)
 48 uses an elliptic yield surface to eliminate deviatoric strains under isotropic loading conditions.
 49 Since the formulation of these yield surfaces is isotropic, their elastic region is quite large. To
 50 improve predictions for different stress increment directions, Vermeer (1978) developed a
 51 double-hardening model for sand consisting of a nonlinear surface for deviatoric yielding (non-
 52 associated) and a separate vertical surface (associated) for volumetric yielding (Fig. 1c). The
 53 formulation in Vermeer's model is also isotropic and thus more appropriate for monotonic
 54 loading conditions. Lade and Kim developed a teardrop shaped model (Fig. 1d) that eliminated
 55 the sharp corner in Vermeer's double hardening model, and some of the associated return
 56 mapping difficulties at the cost of slightly less accurate predictions.



57

58 **Fig. 1. Examples of yield surfaces, $f = 0$, used for geotechnical applications (a) Mohr-Coulomb and**
 59 **Drucker-Prager; (b) Original and modified Cam-clay (Roscoe and Schofield, 1963 and Roscoe and**
 60 **Burland, 1968); (c) Vermeer's Double hardening model (Vermeer, 1978); (d) Tear drop shaped surface**
 61 **from Lade and Kim (1988), (e) Cam-clay bubble model (Al-Tabbaa and Muir Wood (1989), and**
 62 **(f) Drucker-Prager type kinematic hardening surfaces, Poorooshasb and Pietruszczak (1985), Dafalias**
 63 **and Manzari (2004), and SANISAND (Taiebat and Dafalias, 2008)**

64 Yield surfaces that exhibit isotropic hardening, such as those in Figs. 1b, c, and d result in a
65 large elastic region after significant yielding, rendering the models inappropriate for reverse or
66 cyclic loading conditions. To more accurately model cyclic behavior, Mróz et al. (1979)
67 proposed a modeling technique based on kinematic hardening, that translates and rotates during
68 loading, generally within the context of a larger bounding surface that exhibits isotropic and/or
69 kinematic hardening (Fig. 1e). Examples include the Cam-clay bubble model developed by Al-
70 Tabbaa and Muir Wood (1989) for clays (Fig. 1e) in which a small “bubble” yield surface
71 moves inside of an isotropic bounding surface. Both the yield and bounding surfaces have the
72 shape of the modified Cam-clay model. A similar approach for sands includes the Dafalias and
73 Manzari (2004) model, that utilizes a small Drucker-Prager type yield surface, along with a
74 Drucker-Prager type bounding surface, critical state line, and dilatancy surface (Fig. 1f). The
75 model lacks a volumetric cap, and therefore exhibits only elastic volumetric strains upon
76 loading at a constant stress ratio. Taiebat and Dafalias (2008) developed a SANISAND model
77 that uses a rounded yield surface in conjunction with a Drucker-Prager type bounding surface
78 that permits plastic volumetric strains upon loading at constant stress ratio (Fig. 1f). Since
79 kinematic plasticity models often utilize an isotropic bounding surface formulation, and are
80 often calibrated using monotonic tests, the yielding and plastic flow during monotonic loading
81 is important to understand.

82 Interestingly, although the shape of their yield surfaces are notably different, all these models
83 have been shown, by their authors, to produce reasonable predictions for monotonic
84 conventional laboratory tests. It suggests that the input parameters can be tuned to compensate
85 for differences between the experimental and theoretical yield surfaces and flow rules. The
86 appropriateness of the slope of the yield surface is nevertheless very important for the accurate
87 predictions of problems involving more complex stress paths. For instance, if a normally
88 consolidated soil is subject to plastic shear loading followed by a significant increase in pore

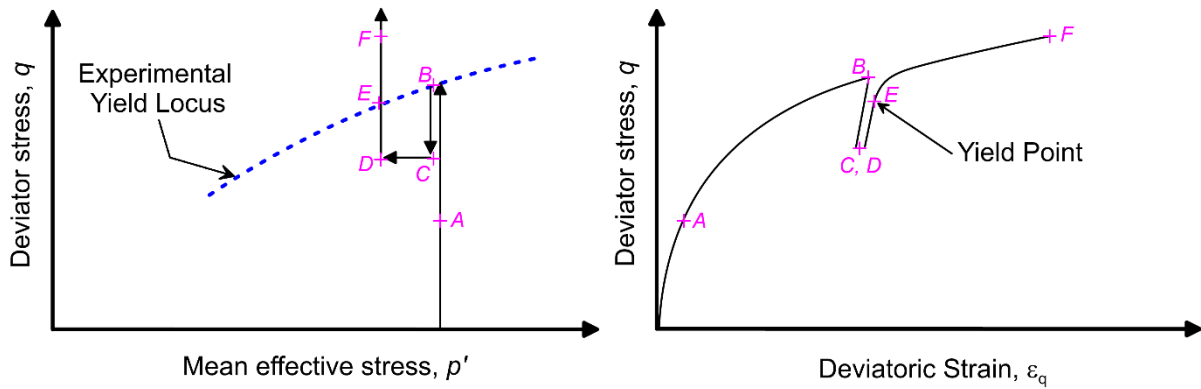
89 water pressure under sustained shear, the predicted behavior during the initial stress increment
90 would be:

- 91 • Elastic according to Cam-clay (Fig. 1b) and conventional Cap (e.g., Baladi and Rohani,
92 1979) models;
- 93 • Plastic according to Double hardening, Dafalias and Poorooshasb models (Figs. 1c and
94 1d), which would result in irrecoverable strains.
- 95 • Elastic or plastic depending on the stress level according to models having tear-drop
96 shaped surfaces (Fig. 1e).

97 **Experimental Studies to Measure Yield and Plastic Potential Surfaces**

98 Although numerous expressions have been proposed for the yield surface ($f = 0$) and plastic
99 potential ($g = 0$) by geotechnical researchers, there are relatively few experimental studies that
100 have attempted to determine their actual shape. Previous experimental studies can be classified
101 according to the following categories:

- 102 1. Tests containing cycles of loading, unloading and reloading (e.g., Poorooshasb et al.,
103 1966 and 1967, Poorooshasb, 1971, Tatsuoka and Ishihara, 1974, Tatsuoka and
104 Molenkamp, 1983, Pradel et al., 1990, Yasufuku et al., 1991, and Nawir et al., 2003),
105 as exemplified in Fig. 2;
- 106 2. Acoustic emission tests (e.g., Tanimoto et al., 1986);
- 107 3. Tests in which the strain path is suddenly changed and plastic strains, slopes as well as
108 moduli are calculated (e.g., Pradel and Lade, 1990, Kuwano and Jardine, 2007);



109

110

Fig. 2. Test with cycles of loading and unloading used for the determination of the yield surface

111

112

113

114

115

116

117

118

Generally, studies belonging to the first group have been used to investigate what Tatsuoka (2006) describes as “large-scale shear yielding”, and have produced open-type yield surfaces with shapes that are similar to the ones in Figs. 1c and 1e. Size and mode of shearing can affect the yield surfaces as cautioned in Tatsuoka and Molenkamp (1983). More recent studies by Nawir et al. (2003) have focused on viscous effects by imposing distinct strain rates during cycles of loading and reloading. The method is powerful, however, the tests necessary tend to be numerous, complex, and require careful interpretation. Interpretation can be especially difficult when:

119

120

121

122

- The mean effective stress, p' , increases significantly, which results in both shear and volumetric yielding mechanisms according to double hardening models (Fig. 1c);
- The unloading cycles produce large loops and irrecoverable strains;
- Yielding occurs near the failure line and mobilizes large strains.

123

124

125

126

127

The use of acoustic emissions to determine the shape of the yield surface requires not only specialized equipment (e.g., Tanimoto and Tanaka, 1986), but also requires sufficient noise generated by slippage and/or crushing of soil particles to accurately differentiate ambient noise from the acoustic emissions generated by yielding. Hence, the contributions from this methodology have been relatively limited.

128 The third methodology was used by Kuwano and Jardine (2007) to study kinematic yielding
129 and Pradel and Lade (1990) to study the conditions leading to static liquefaction of saturated
130 and partly saturated sands at a specific state of stress. Both studies involved a large number of
131 tests. For example, Pradel and Lade (1990) used a total of four triaxial tests from which moduli
132 were measured to obtain the slopes of the yield and plastic potential surfaces at a single point
133 in the $q - p'$ plane. Hence, the applicability of these methods to a wide range of stresses is
134 generally not practical.

135 The main purpose of the present study is to extend the work by Pradel and Lade (1990) to
136 experimentally obtain the slopes of the yield and plastic potential surfaces. This method is
137 based on the incremental formulation of the deformation (or flow) theory of plasticity, and
138 incorporates short undrained perturbations during a drained triaxial test with a vertical stress
139 path. The tests can be performed on a traditional triaxial compression testing device without
140 the need for specialized equipment, which makes the method attractive for routine use.

141 **Incremental Formulation and Theoretical Background**

142 The deformation theory of plasticity (e.g., Jones, 2009 and Wood, 1990) postulates that strains
143 can be decomposed into elastic (fully recoverable) and plastic (irrecoverable) components. For
144 a time-independent material this postulate is expressed incrementally as in Eq. 1.

$$d\varepsilon_{ij} = d\varepsilon_{ij}^e + d\varepsilon_{ij}^p \quad (1)$$

145 The theory of plasticity also postulates that a boundary exists in the stress space between elastic
146 and plastic behavior. This boundary, namely the yield surface, is defined by a mathematical
147 function, f , that describes a convex surface in the six-dimensional stress space as $f(\sigma_{ij}) = 0$.
148 During loading (yielding), the direction of the plastic strain increments is perpendicular to a
149 plastic potential surface, defined by a mathematical function, g , as $g(\sigma_{ij}) = 0$. Plastic loading

150 resulting from an effective stress increment, $d\sigma_{ij}$, results in the plastic strain increment given
 151 in Eq. 2 (Pradel and Lade, 1990).

$$d\varepsilon_{ij}^p = \frac{1}{h} \frac{\partial g}{\partial \sigma'_{ij}} \frac{\partial f}{\partial \sigma'_{kl}} d\sigma'_{kl} \quad (2)$$

152 Where, h , is the plastic hardening modulus (which is a function of hardening variables such as
 153 void ratio, previous stress history, stress and strain invariants, etc.).

154 In most elastoplastic models, the surfaces f and g are expressed in terms of invariants, and for
 155 conventional triaxial compression tests these surfaces can be defined uniquely in terms of the
 156 stress invariants provided in Eq. 3. Where p' is mean effective stress and q is the deviatoric
 157 stress.

$$p' = \frac{1}{3}(\sigma'_1 + \sigma'_2 + \sigma'_3) \quad (3a)$$

$$q = \sqrt{\frac{1}{2}[(\sigma'_1 - \sigma'_2)^2 + (\sigma'_1 - \sigma'_3)^2 + (\sigma'_2 - \sigma'_3)^2]} \quad (3b)$$

158 Similarly, the volumetric and deviatoric strain invariants are defined as:

$$\varepsilon_v = \varepsilon_1 + \varepsilon_2 + \varepsilon_3 \quad (4a)$$

$$\varepsilon_q = \frac{2}{3} \sqrt{\frac{1}{2}[(\varepsilon_1 - \varepsilon_2)^2 + (\varepsilon_1 - \varepsilon_3)^2 + (\varepsilon_2 - \varepsilon_3)^2]} \quad (4b)$$

159 Elastic deviatoric and volumetric and strains can be computed using G and K , the elastic shear
 160 and bulk moduli using Eqs. 5 (a) and (b), respectively.

$$d\varepsilon_q^e = \frac{dq}{3G} \quad (5a)$$

$$d\varepsilon_v^e = \frac{dp'}{K} \quad (5b)$$

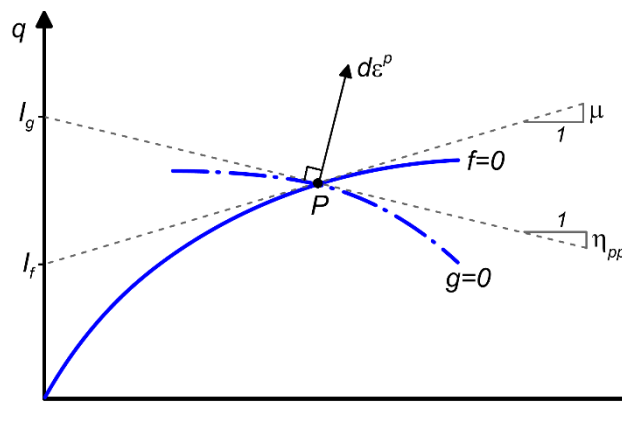
161 The introduction of local linear approximations for the yield surface (e.g., $f = q - \mu \cdot p' - I_f = 0$)
 162 and plastic potential (e.g., $g = q - \eta_{pp} \cdot p' - I_g = 0$), adopted from Fig. 3, into equation (2)
 163 provides the expressions provided in Eqs. (6a) and (6b), for the deviatoric and volumetric
 164 strains during plastic loading, respectively. Note that the I_f and I_g are intercepts of the slope of
 165 the yield surface and the plastic potential with the y-axis in Fig. 3.

$$d\varepsilon_q^p = \frac{1}{h} \frac{\partial g}{\partial q} \left(\frac{\partial f}{\partial q} dq + \frac{\partial f}{\partial p'} dp' \right) = \frac{1}{h} (dq - \mu \cdot dp') \quad (6a)$$

$$d\varepsilon_v^p = \frac{1}{h} \frac{\partial g}{\partial p'} \left(\frac{\partial f}{\partial q} dq + \frac{\partial f}{\partial p'} dp' \right) = \frac{-\eta_{pp}}{h} (dq - \mu \cdot dp') \quad (6b)$$

166 Where μ and η_{pp} are tangent slopes of the yield and plastic potential surfaces in the $q - p'$ plane
 167 at the current stress point, shown in Fig. 3. As presented by Pradel and Lade (1990), the total
 168 strains are obtained by summing the elastic and plastic strain increments, provided in Eq. 7.

$$\begin{pmatrix} d\varepsilon_q \\ d\varepsilon_v \end{pmatrix} = \begin{pmatrix} \left(\frac{1}{3G} + \frac{1}{h} \right) & \frac{-\mu}{h} \\ \frac{-\eta_{pp}}{h} & \left(\frac{1}{K} + \frac{\mu \cdot \eta_{pp}}{h} \right) \end{pmatrix} \cdot \begin{pmatrix} dq \\ dp' \end{pmatrix} \quad (7)$$



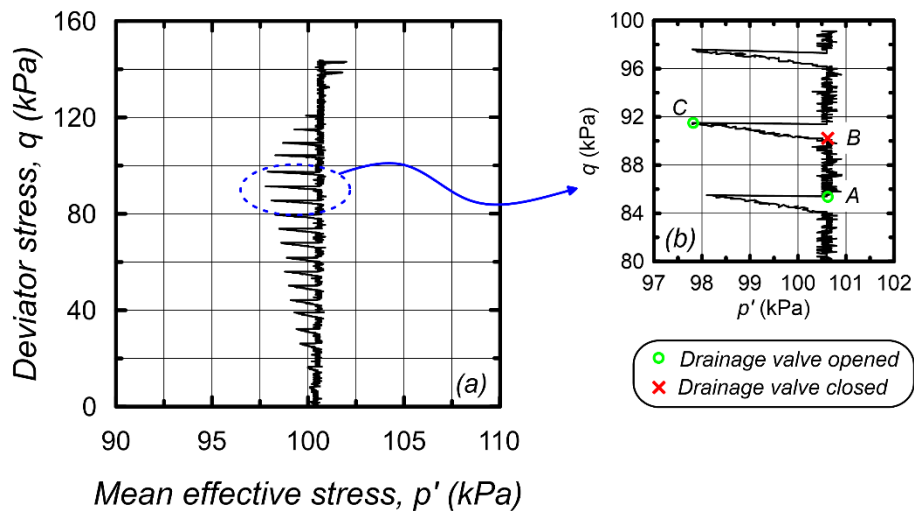
169
 170 **Fig. 3. Schematic representation of the yield surface, plastic potential and the gradients to these surfaces**
 171 **and the plastic strain increment at point P in the triaxial space**

172 **Experimental Application**

173 During loading equation (7) provides two equations that are derived from the five elastoplastic
174 material properties: G , K , h , μ , and η_{pp} . Though Eq. 7 is strictly applicable at a single point, it
175 is approximately valid for small stress increments within the region where the linearized form
176 is approximately equivalent to the surfaces. To measure these properties, first the elastic
177 moduli, G and K , are measured using small volumetric and deviatoric load paths, or another
178 suitable means such as bender element tests. Because G and K depend on p' for soil,
179 maintaining a constant value of p' is advantageous during shearing. To measure h , μ , and η_{pp} ,
180 a triaxial compression test (as illustrated in Fig. 4) is performed using the following steps:

- 181 1. A vertical stress path is first applied under drained loading conditions (points A to B in
182 Fig. 4), and values of $d\varepsilon_q$, $d\varepsilon_v$, and dq are measured;
- 183 2. The drain valve is closed to provide a small undrained perturbation (e.g., between points
184 B to C in Fig. 4), and values of $d\varepsilon_q$, dq , and dp' are measured.
- 185 3. The drain valve is slowly opened (at point C).

186 The process described above is repeated at multiple points along the stress path.



187

188 **Fig. 4. Stress path of drained p' constant triaxial test with a short undrained portion (note that the scale**
189 **of the horizontal axis has been stretched for illustrative purposes)**

190 During the drained shearing phase, values of h and η_{pp} are computed using Eqs. 8 and 9,
 191 respectively, which are obtained by solving Eq. 7 with $dp' = 0$.

$$h = \frac{1}{\frac{d\varepsilon_q}{dq} - \frac{1}{3G}} \quad (8)$$

$$\eta_{pp} = -\frac{d\varepsilon_v}{dq} h \quad (1 \quad 9)$$

192 The value of μ is solved from the undrained loading phase using Eq. 10, obtained after making
 193 appropriate substitutions into the portion of Eq. 7 corresponding to $d\varepsilon_q$ (i.e., the top line in the
 194 equation), and using the value of h from Eq. 8.

$$\mu = \left[\left(1 + \frac{h}{3G} \right) \frac{dq}{dp'} - \frac{d\varepsilon_q}{dp'} \right] \quad (10)$$

195 Note that $d\varepsilon_v = 0$ for undrained loading (i.e., the bottom line of Eq. 7) provides an expression
 196 for a residual that should equal zero, and therefore provides a means of assessing the quality of
 197 the measurements. The resulting residual equation is given by Eq. 11.

$$0 \approx R = \frac{-\eta_{pp}}{h} dq + \left(\frac{1}{K} + \frac{\mu \cdot \eta_{pp}}{h} \right) dp \quad (11)$$

198

199 **Experimental Results**

200 A GCTS STX-50 pneumatic triaxial device was utilized to perform the experiments presented
 201 herein. The device is equipped with an internal load cell so that friction between the piston and
 202 the bushing is not included in the vertical force measurement. Vertical displacements were
 203 measured using an LVDT mounted on the piston outside of the cell. Volume change was
 204 measured by a differential pressure transducer measuring the difference in pressure between
 205 the top and bottom of the burette. The stock burettes that come with the device have a diameter

206 of 17.4 mm, which is rather large. To enhance the accuracy of the volume change
207 measurements, a smaller burette with a diameter of 6.3 mm was installed on the device. Pore
208 pressure was measured using a pressure transducer installed between the bottom of the
209 specimen and the valve on the line coming out of the cell. This position avoids errors in volume
210 change arising from volumetric compliance of the plastic tubes connecting the specimen to the
211 burettes.

212 The cylindrical specimens had a height of 150mm and a diameter of 71mm. The rubber latex
213 membranes used were 0.5mm thick. The top and bottom platens of the triaxial apparatus were
214 not lubricated, which may contribute to experimental errors due to shear stresses on the top and
215 bottom surfaces. Membrane penetration was not measured, but is expected to be small because
216 the sand is fine relative to the membrane thickness. More detailed documentation on laboratory
217 procedures are provided in Eslami (2017).

218 The triaxial test configuration utilized herein is fairly standard, and can be replicated in many
219 laboratories. This makes the procedure presented herein approachable for routine application.
220 The influence of measurement errors is quantified by calculating confidence limits on the
221 computed plasticity parameters. The confidence limits include the influence of measurement
222 noise on the computed quantities. More advanced measurement techniques, such as internal
223 displacement or strain measurements, lubricated top and bottom caps, or image analysis of the
224 surface displacement field could improve the data quality, thereby reducing the range of the
225 confidence limits. Although these techniques are common in Japanese laboratories they are less
226 common in the US and other countries, and were not applied in the current study.

227 The experimental results derived from this study are curated, published (Eslami et al. 2017),
228 and available for re-use in DesignSafe-CI, a platform for natural hazards research (Rathje et
229 al., 2017). The interactive data curation and publication pipelines permits assigning categories

230 to data to represent the primary processes of engineering experiments (Esteva et al., 2016). The
231 dataset contains the experimental data, as well as more detailed documentation on laboratory
232 procedures. A Jupyter notebook is also included to facilitate visualization of the data.

233 **Tested Material and Sample Preparation**

234 The material tested was a clean “Orange County Silica sand-mesh 60”, with a mean grain size
235 D_{50} , of 0.3 mm, a coefficient of uniformity $C_u = 2$ and a coefficient of curvature $C_c = 1.24$. This
236 sand classifies as SP according to the Unified Soil Classification System (ASTM D2487). The
237 minimum and maximum void ratios for the sand were $e_{min} = 0.792$ and $e_{max} = 0.958$. The slope
238 of the yield surface depends on the measurement of pore pressure change during small
239 undrained perturbations. To enhance the pore pressure response, the specimens were prepared
240 as loose as possible. A plastic tube with a fine mesh at the bottom was first inserted into the
241 specimen mold with the mesh resting on the bottom porous stone. The outside diameter of the
242 tube was slightly smaller than the inside diameter of the triaxial mold. Dry sand was then placed
243 into the plastic tube, and the tube was raised very slowly so that the sand particles were
244 pluviated at essentially zero drop-height. The average void ratio of the dry samples prior to
245 consolidation was 0.955, which corresponds to a relative density of about 2% prior to testing.
246 The samples were subsequently isotropically consolidated, which caused the relative density
247 to increase slightly but still remain under 10%. Samples were flushed with CO₂ prior to
248 saturation with de-aired water, and back pressure saturation was used to achieve B-values
249 larger than 95%. The average saturated unit weight of the samples was 18.1 kN/m³, and their
250 dry unit weight was on average 13.3 kN/m³.

251 **Elastic Moduli**

252 To measure the elastic bulk modulus, K , a specimen was isotropically consolidated to 100 kPa,
253 and the cell pressure was then cyclically reduced to 80 kPa and increased to 100 kPa while the

254 volume change was recorded using a differential pressure transducer. The bulk modulus was
255 computed using Eq. 5b. This process was repeated as the specimen was isotropically
256 consolidated to 200, 300, 400, 300, 200, and 100 kPa. The resulting bulk modulus values are
257 plotted in Fig. 5. A least-squares regression was performed to relate bulk modulus to mean
258 effective stress, as indicated in Eq. 12a, where $p_a = 101.325$ kPa.

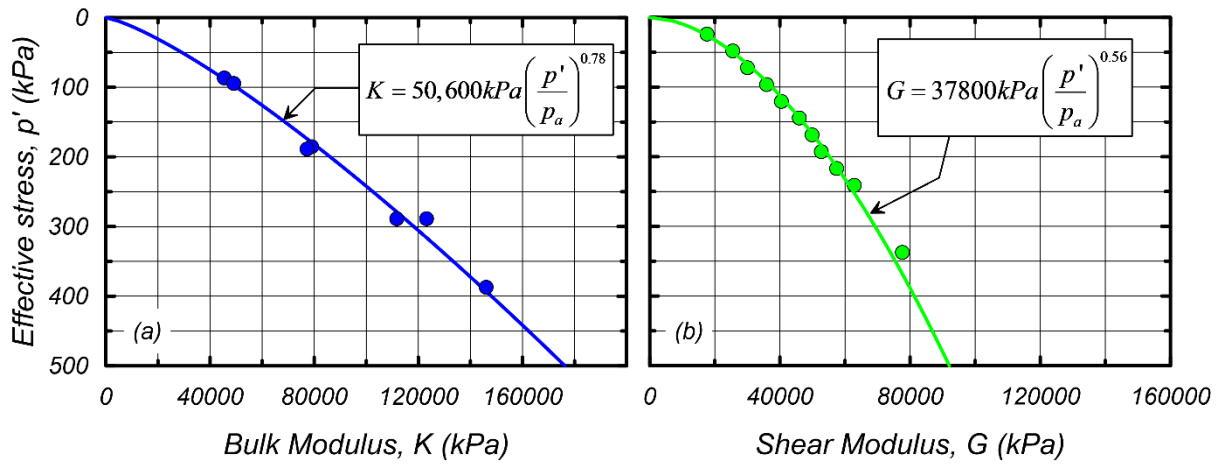
259 To measure shear modulus, two methods were considered. First, the Young's modulus, E , was
260 measured by imposing 0.01% amplitude cyclic axial strain cycles, computing the slope by least
261 squares regression, and subsequently computing shear modulus as $G = 3KE/(9K-E)$, in
262 accordance with homogeneous isotropic linear elasticity theory, where the measured values of
263 K and E corresponding to each consolidation pressure were used. This method is not
264 particularly accurate because (1) the cyclic strain amplitude is large enough that the measured
265 response is a combination of elastic and plastic behavior, and separating the two responses
266 requires additional assumptions, and (2) sensor noise contributed significantly to the
267 measurements because 0.01% is close to the resolution limit for the load cell and LVDT.
268 Therefore, the shear modulus was measured using bender elements embedded in the sand using
269 a custom-made consolidation ring. Vertical pressures were applied to the sand, the source
270 bender element was excited by a step wave function, and the travel time was selected based on
271 the received signal following procedures outlined by Brandenburg et al. (2008). The bender
272 element excitations are very small strain, and therefore act in the elastic region of the soil. The
273 measurements were then regressed to obtain Eq. 12(b). The adopted values of the shear
274 modulus are shown in Eq. 12b and Figure 5.

275

$$K = 50,600kPa \left(\frac{p'}{p_a} \right)^{0.78} \quad (12a)$$

276

$$G = 37,800kPa \left(\frac{p'}{p_a} \right)^{0.56} \quad (12b)$$



277

278 **Fig. 5. Measurements of elastic moduli experiment: (a) bulk modulus measurements and adopted**
 279 **correlation, (b) Shear modulus measurements and correlation**

280

281 Shear Testing

282 Testing was conducted for mean effective consolidation stress values of $p' = 100, 150, 200,$
 283 $250, 300, 350$ and 400 kPa, and the resulting stress paths are plotted in Fig. 6. Constant mean
 284 effective stress conditions were obtained using stress-controlled loading and by decreasing the
 285 cell pressure as follows: $\Delta\sigma_3 = -q/3$. A computer control system was utilized to achieve the
 286 desired stress path. During drained loading, the drain tap connected to the specimen was
 287 periodically closed to impose a small undrained loading perturbation on the specimen. These
 288 perturbations manifest as sudden changes in p' apparent in Fig. 6. The drain tap was left closed
 289 until adequate pore pressure response had been recorded, and subsequently re-opened very
 290 slowly to proceed with drained loading. Approximately 20 to 25 perturbations were imposed
 291 on each specimen. The perturbations resulted in a small reduction in p' at low stress ratios
 292 where the specimens were contractive. However, the specimens became slightly dilative at
 293 stress ratios (q/p') higher than about $M^d = 1.3$ (Fig. 6a).

294 Note that M^d is the stress ratio at the transition from contractive to dilative behavior. The tests
295 reached deviatoric strains of 10%, at which point the deviatoric stress and void ratio were still
296 changing as deviatoric strain increased, indicating that the specimens did not reach a critical
297 state condition. The stress ratio at a strain of 10% was $M = q/p' = 1.4$, which is associated with
298 a friction angle of $\phi = 34^\circ$, where $M = 6 \sin \phi / (3 - \sin \phi)$.

299 The values of dq/dp' , $d\varepsilon_q/dp'$, $d\varepsilon_q/dq$, and $d\varepsilon_v/dq$ required to solve for h , η_{pp} , and μ using Eqs.
300 8, 9, and 10, respectively, were obtained as illustrated in Fig. 7 for one of the perturbations
301 conducted at a consolidation stress of 400 kPa. The quantities were first plotted versus time,
302 and the rates of change of each quantity were computed using linear least squares regression
303 for the load increment both the drained and undrained portions of loading. The rate dp'/dt was
304 set to zero during drained loading and $d\varepsilon_v/dt$ was set to zero for undrained loading. The desired
305 ratios were then computed as the ratio of the rates [e.g., $dq/dp' = (dq/dt)/(dp'/dt)$]. The number
306 of data points extracted for linear least squares regression depended on the amount of
307 nonlinearity in the soil response. Near the beginning of each test (i.e., at low stress ratio) more
308 data points were utilized because the strains evolved more slowly than later in the test. Recall
309 that stress control was required to maintain a vertical stress path, therefore the strain rate tended
310 to increase with time as the soil became softer.

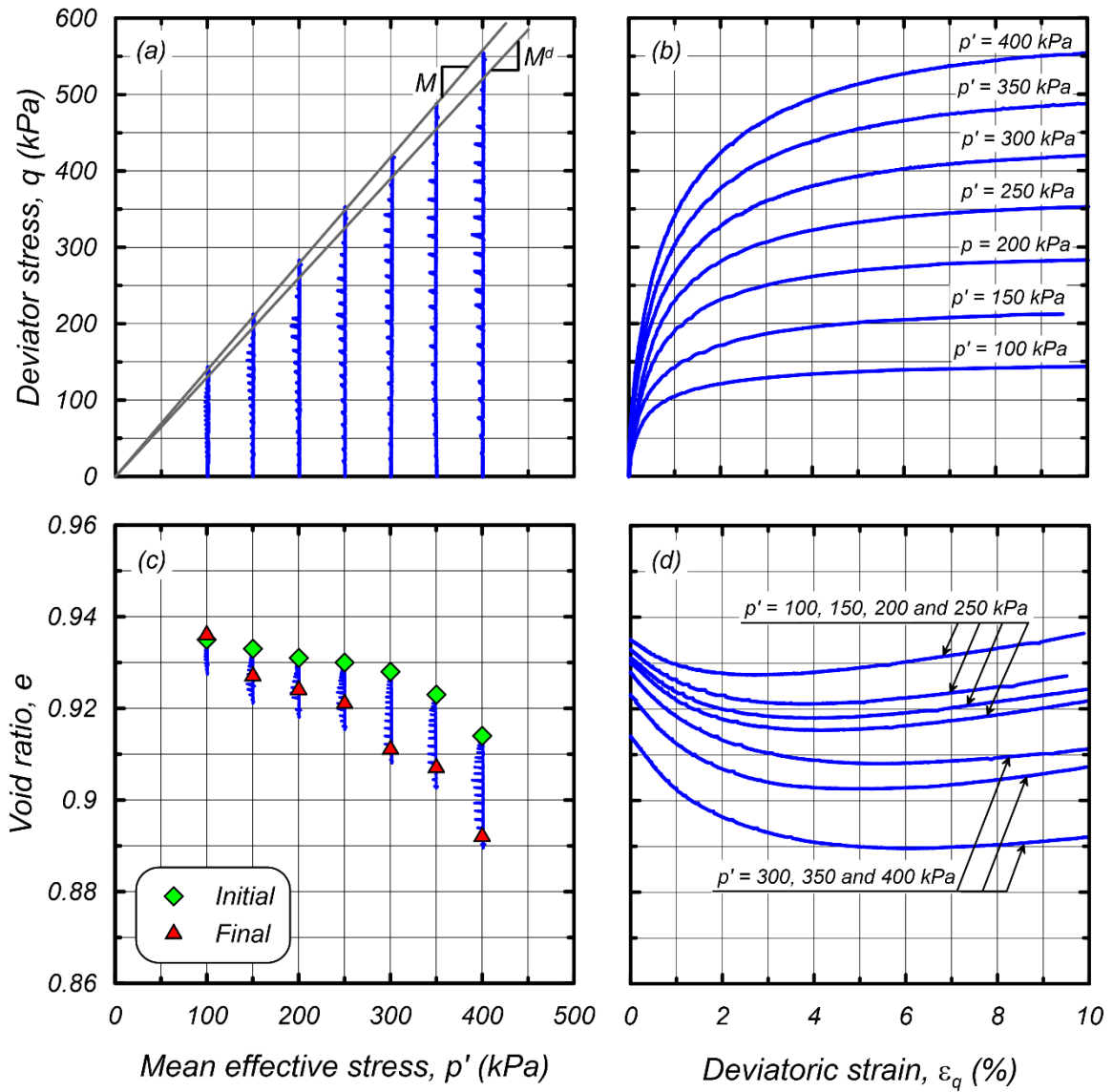
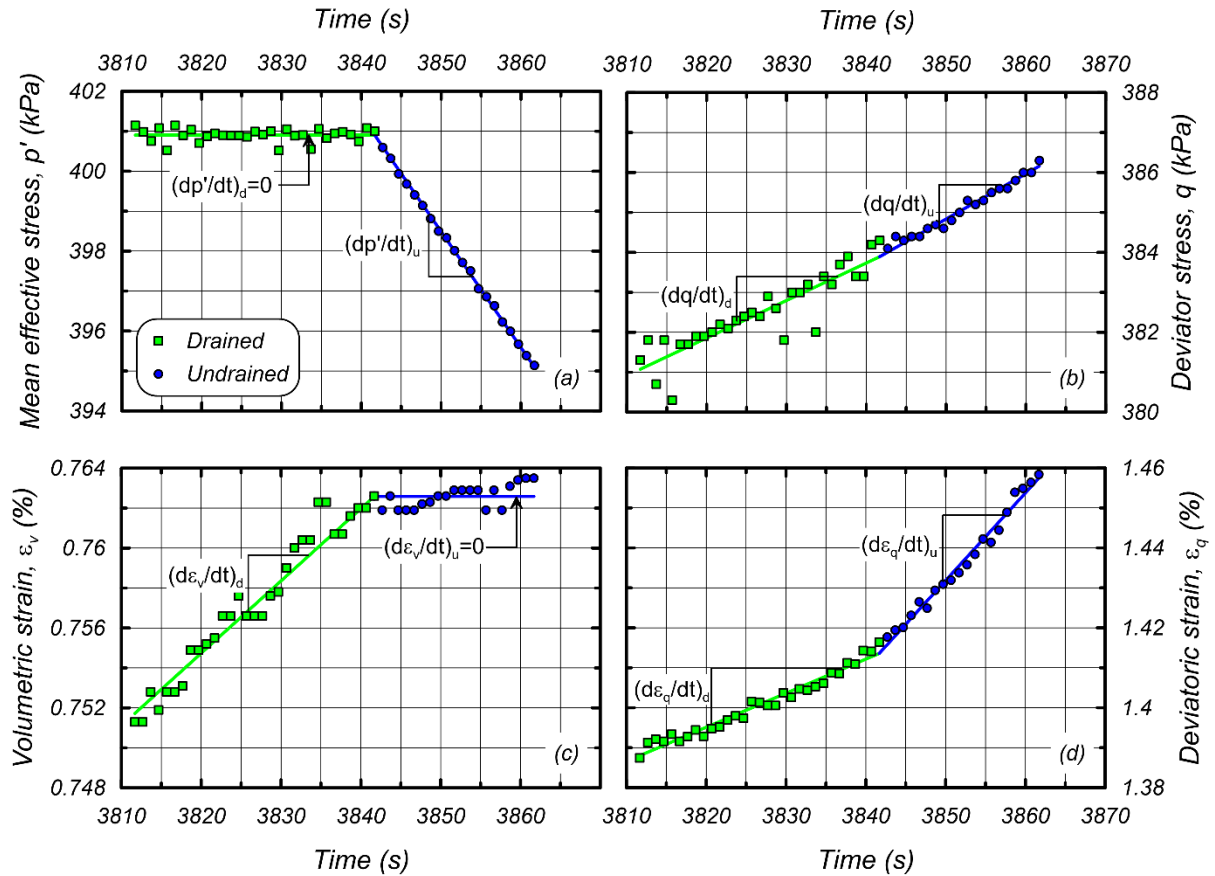


Fig. 6. General soil behavior of 7 triaxial compression tests: (a) effective stress paths, (b) stress-strain curves, (c) void ratio vs. mean effective stress, (d) void ratio vs. deviatoric strain curves

311
 312
 313
 314



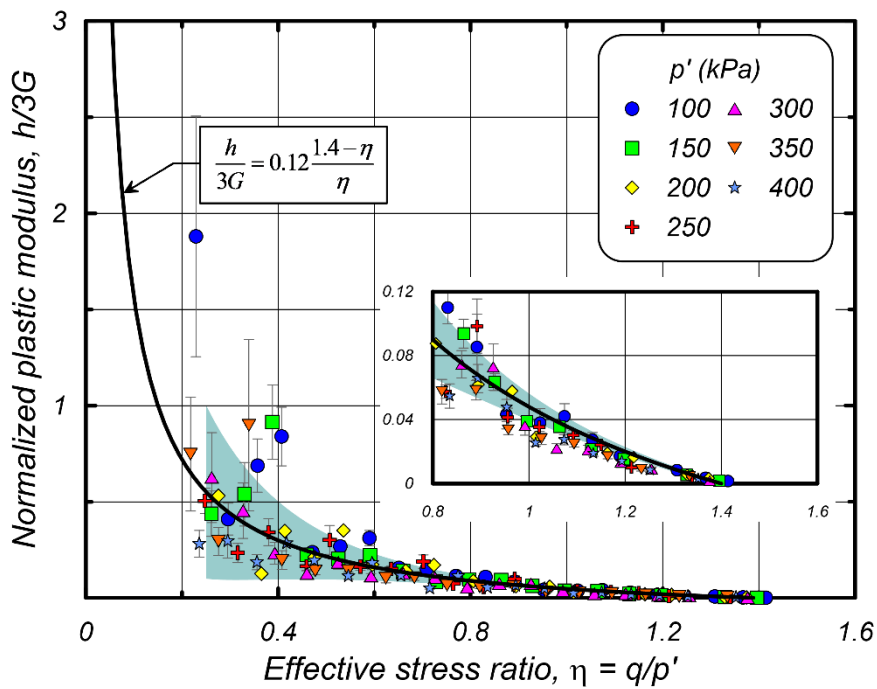
315
 316 **Fig. 7. Example data during one perturbation for the specimen consolidated at 400 kPa. Data quantities**
 317 **are (a) mean effective stress, (b) deviator stress, (c) volumetric strain, and (d) deviatoric strain.**

318 **Plastic Modulus**

319 A value of plastic modulus was computed from the drained loading stages based on Eq. 8 at
 320 each point where an undrained perturbation was imposed on the specimen. The resulting plastic
 321 modulus values were subsequently normalized by $3G_c$, and plotted in Fig. 8. Plastic modulus is
 322 known to depend on shear modulus (e.g., Dafalias and Manzari, 2004), hence normalizing the
 323 plastic modulus results in a relationship that is independent of p' . The 95% confidence limits
 324 indicate that the measurements were of poorer quality at low stress ratio than at high stress
 325 ratio. This is due to the fact that deviatoric strain increments are quite small at low stress ratio,
 326 therefore signal noise influences the measurement of h . A weighted least squares regression
 327 was performed to arrive at Eq. 13, where weights were assigned to be inversely proportional to
 328 the 95% confidence limit range.

329
$$\frac{h}{3G} = 0.12 \frac{1.4 - \eta}{\eta} \quad (13)$$

330 The functional form of the expression above, assumes that plastic modulus is inversely
 331 proportional to the distance from the current point in q - p' space to the failure line, M . This
 332 loosely follows Dafalias and Manzari (2004), with the exception that they compute plastic
 333 modulus as a function of distance to the bounding surface, which in turn depends on the state
 334 parameter. The constants 1.4 and 0.12 are analogous to the parameters M^b (the bounding or
 335 “image” stress ratio on the bounding surface) and b_0 (a parameter that defines the plastic
 336 modulus at the initiation of the loading process) in Dafalias and Manzari (2004), respectively.



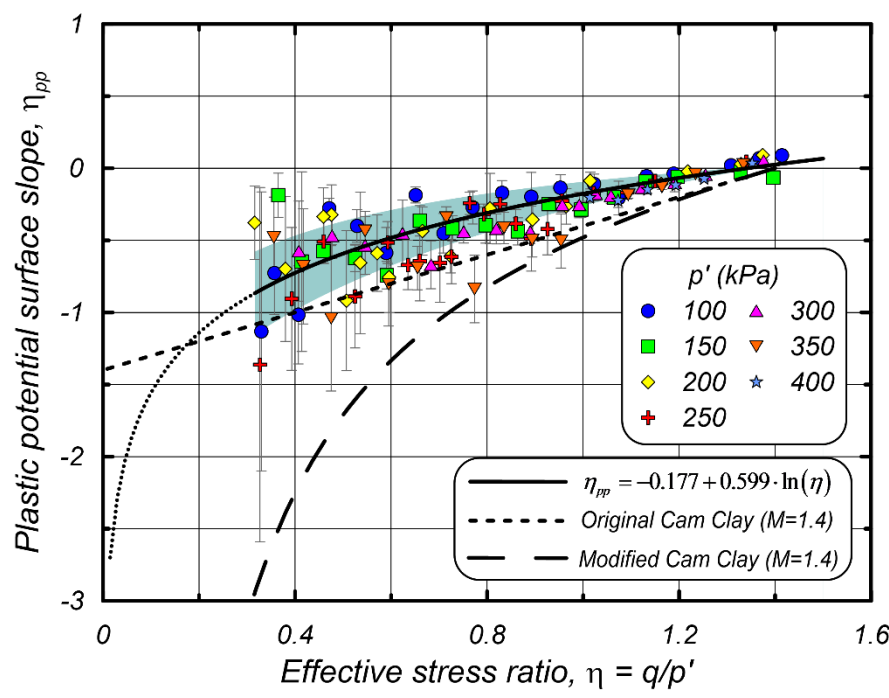
337
 338 **Fig. 8. Normalized plastic modulus ($h/3G$) versus stress ratio ($\eta = q/p'$). Vertical bars are 95%**
 339 **confidence limits and shaded region corresponds to \pm one standard deviation of the residuals.**

340 **Plastic Potential Slope**

341 The slope of the plastic potential surface, η_{pp} , was computed for each undrained perturbation,
 342 and the results are plotted versus the stress ratio $\eta = q/p'$ in Fig. 9. A negative slope of the
 343 plastic potential surface indicates contractive behavior, while a positive slope indicates dilation.

344 The sand is contractive essentially over the full range of loading, and is the most highly
 345 contractive at a stress ratio near 0.4. Superposed on the data are the slopes of the plastic
 346 potential surfaces associated with the original and modified Cam-clay models (Schofield and
 347 Wroth, 1968, and Roscoe and Burland, 1968). Although the Cam-clay model was formulated
 348 for clay and not for sand, the sand tested herein appears to exhibit characteristics that are
 349 qualitatively similar to the Cam-clay model. This does not mean that the Cam-clay model is
 350 appropriate for sands because the compressibility behavior may in fact be significantly
 351 different. The original Cam-clay model has a slope that varies linearly with η , and fits the
 352 observed data reasonably well at stress ratios higher than about 0.8, but lies beneath the data at
 353 lower stress ratios. The modified Cam-clay model lies significantly below the data. A weighted
 354 least squares regression was performed on the data, resulting in the expression given in
 355 equation (14).

356
$$\eta_{pp} = -0.177 + 0.599 \cdot \ln(\eta) \tag{14}$$



357
 358 **Fig. 9. Slope of plastic potential surface, η_{pp} , versus effective stress ratio ($\eta = q / p'$). Vertical bars are**
 359 **95% confidence limits and shaded region corresponds to \pm one standard deviation of the residuals.**

360

361 Flow behavior is known to depend not only on stress ratio, but also on the void ratio relative to
 362 the critical state void ratio, which is commonly quantified by the state parameter $\psi = e - e_c$. For
 363 example, the tested specimens were more highly contractive at high p' where ψ was largest
 364 (Fig. 6c). To account for the influence of soil state on plastic flow, the plastic potential surface
 365 must be a function not only of η , but also ψ . The data were therefore regressed according to
 366 the functional form in Eq. 15 (following Dafalias and Manzari 2004), with the results:
 367 $A_d = 0.61$ and $n_d = 11.2$. Since the specimens did not reach critical state, the critical state void
 368 ratio is unknown. For simplicity, the state parameter was therefore computed as the difference
 369 between the current void ratio and final void ratio for the test. Furthermore, $M = 1.4$ was used.

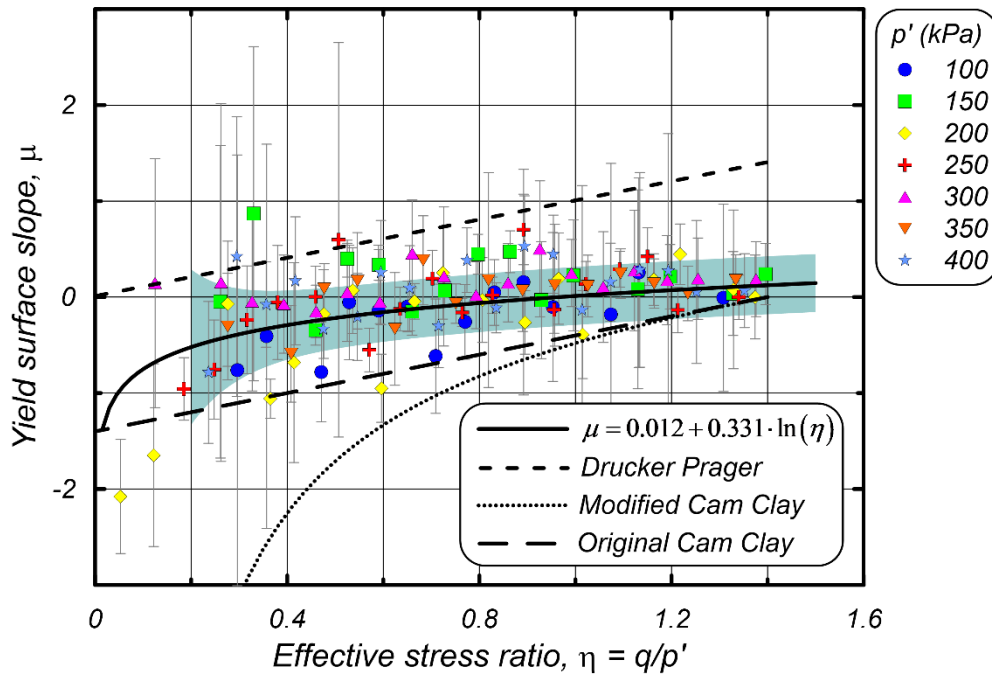
$$370 \quad \eta_{pp} = -A_d \left[M \cdot \exp(n_d \cdot \psi) - \eta \right] \quad (15)$$

371 **Yield Surface Slope**

372 The slope of the yield surface is plotted versus stress ratio in Fig. 10. The yield surface is
 373 negative at low stress ratio, and increases with stress ratio becoming positive at about $\eta = 1.1$.
 374 The 95% confidence limits are larger for the yield surface slope than for the plastic potential
 375 slope because the yield surface slope calculation utilizes volumetric strain, which is a
 376 comparatively noisy measurement, and carries over measurement errors from h and η_{pp} . A
 377 weighted least squares regression results in Eq. 16.

$$378 \quad \mu = 0.012 + 0.331 \cdot \ln(\eta) \quad (16)$$

379 Eq. 16 differs from Eq. 14, which indicates that the sand exhibits a non-associated flow rule.
 380 For comparison, the Modified Cam-clay ($M=1.4$), Original Cam-clay ($M = 1.4$), and Drucker
 381 Prager yield surfaces are provided in Fig. 10. Note that the slope of the Drucker-Prager yield
 382 surface must be equal to the stress ratio for cohesionless material during yielding. None of
 383 these yield surfaces provide a particularly suitable match to the experimental data.



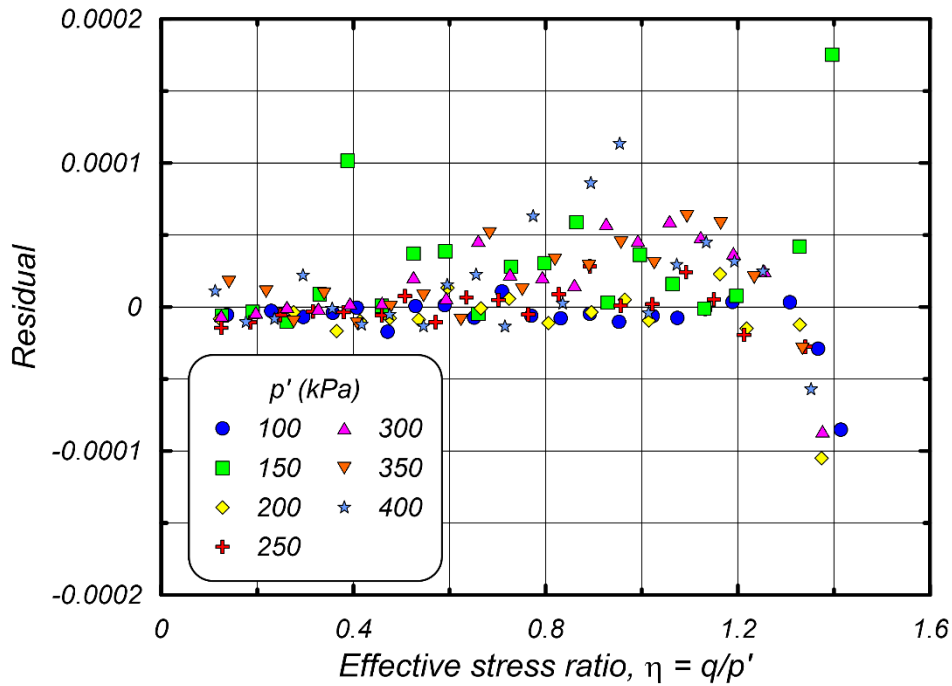
384

385 **Fig. 10. Slope of yield surface, μ , versus effective stress ratio ($\eta = q / p'$). Vertical bars are 95%**
 386 **confidence limits and shaded region corresponds to \pm one standard deviation of the residuals.**

387

388 Residuals

389 Residuals computed using Eq. 11 are plotted in Fig. 11, and have units of volumetric strain. If
 390 the data quantities were measured perfectly, these residual values would be zero. The mean
 391 value of the residuals is $8.7e-6$, and the standard deviation is $3.3e-5$. These numbers are rather
 392 small compared with the measurement accuracy of the volume change sensor. For example,
 393 the noise amplitude of the volume change sensor is about $2.1e-5$, which is close to the standard
 394 deviation of the residuals. This is an indication that we have extracted as much as possible from
 395 the data considering the limitations of the measurements. Any systematic errors (e.g., if the soil
 396 response were nonlinear within the range of measurements extracted for data processing)
 397 would cause these residuals to be higher than the noise levels of the volume change sensor.



398
399 **Figure 11. Residuals, R , computed using Eq. 13 versus effective stress ratio ($\eta = q/p'$)**
400

401 **Interpretation of Data**

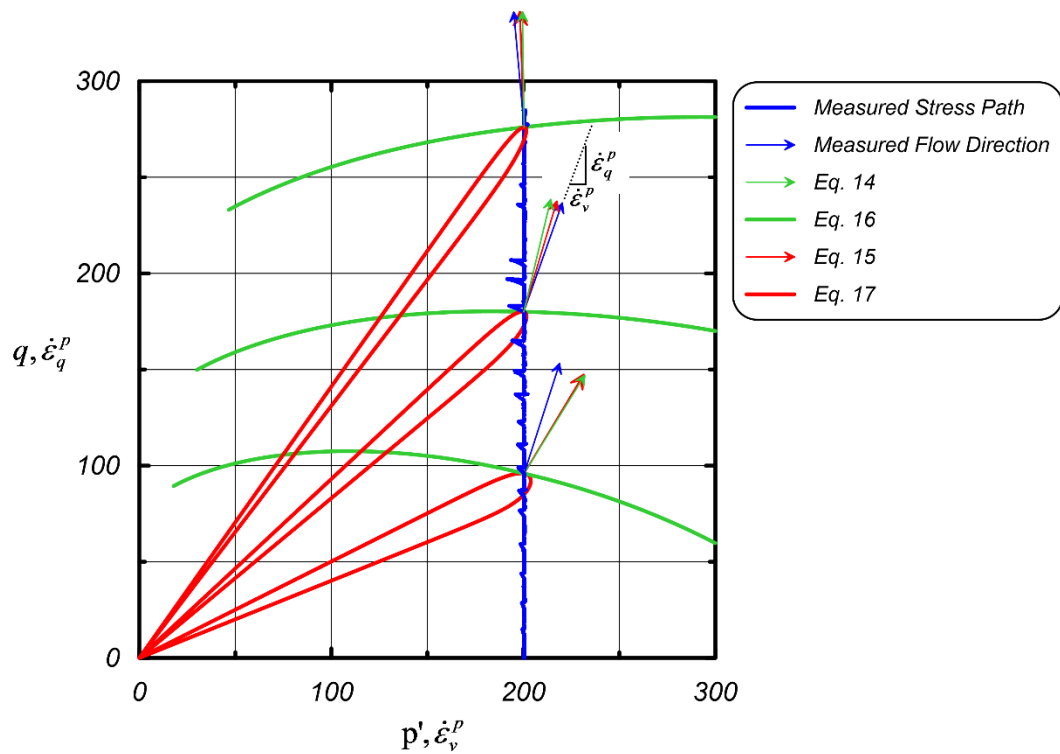
402 The experimental data provide insights into the slopes of the yield and plastic potential
 403 functions. Equations 14, 15, and 16 provide these slopes at a particular point in stress space,
 404 and assumptions are required to sketch the yield or plastic potential surface. The simplest
 405 approach for interpreting the data is to assign a point in stress space, compute the desired slope
 406 at this point, and integrate the slope over a range of stress ratios to sketch the rest of the surface.
 407 This inherently assumes that the surfaces enclose an increasingly large elastic region as loading
 408 progresses (i.e., isotropic hardening). This assumption is similar to many traditional
 409 elastoplastic models such as Cam-clay. An example of this approach is illustrated in Fig. 12
 410 for a vertical stress path at $p' = 200$ kPa, where yield surfaces are sketched at three different
 411 points along the stress path. These lines were obtained by numerically integrating Eq. 16. The
 412 shape of the surfaces is qualitatively similar to the original Cam-clay model in that the surfaces
 413 are curved and skewed to the left. The yield surfaces in Fig. 12 are drawn only in regions that

414 lie reasonably within the bounds of experimental validation. Vectors indicating the directions
415 of plastic flow that were measured, and computed using Eqs. 14 and 15 are also shown in Fig.
416 12 at the points where the stress path intersects the yield surface. The plastic flow vectors are
417 not tangent to the yield surfaces at these points due to the non-associated flow rule.

418 Traditional isotropic hardening models provide reasonable predictions for monotonic loading,
419 but results in a large elastic region that is inappropriate for cyclic loading. Models that utilize
420 small yield surfaces that exhibit kinematic hardening are better suited to capture inelasticity in
421 the reverse direction. For example, SANISAND (Taiebat and Dafalias, 2008) utilizes a narrow
422 closed cone-type yield surface given by Eq. 17. This yield surface equation can be calibrated
423 to match the experimental data by setting the parameters n and m , and solving for α and p_0 that
424 provides the desired yield surface slope at a specific point in stress space. Note that α is the
425 rotational hardening backstress ratio, p_0 is the isotropic hardening variable, m is the tangent of
426 half the opening angle of the yield surface, and the exponent n introduces the effect of a cap-
427 like shape at the tip of the yield surface. SANISAND yield surfaces are shown in Fig. 12 for
428 $m = 0.5$ and $n = 20$. These surfaces intersect the isotropic hardening yield surfaces at the same
429 points and with the same slopes, and provide an alternative interpretation that is equally
430 consistent with the experimental data.

431

$$f = (q - p\alpha)^2 - m^2 p^2 \left[1 - \left(\frac{p}{p_0} \right)^n \right] = 0 \quad (17)$$



432

433 **Fig. 12. Yield and plastic potential surfaces consistent with the experimental data for a vertical stress path**
 434 **at $p' = 200$ kPa**

435 Elastoplastic functions are known to be dependent on loading rate effects. This has been shown
 436 by experimental studies such as Nawir et al. (2003) by mapping the shear yield surface by
 437 changing the strain rate during shear, suggesting that viscous properties be considered for
 438 realistic constitutive modeling of sands. The method described herein can be useful in
 439 evaluating viscous rate effects and for further refinements in sand constitutive modelling.

440 **Conclusions**

441 This paper describes a new experimental method based on the deformation (or flow) theory of
 442 plasticity. The method was used to determine the plastic modulus, and slopes of the plastic
 443 potential and yield surfaces during monotonic shear. The proposed method involves creating,
 444 at regular intervals, small undrained perturbations by closing the drainage valve during shear
 445 for a short time, and computing slopes and moduli at the locations where these perturbations

446 were imposed. The proposed method was applied to an experimental program consisting of
447 triaxial tests on loose uniformly graded sand.

448 For ease of interpretation the specimens were sheared while maintaining a constant mean
449 stress, p , during shear. Note that constant p tests are not a necessity for the use of the proposed
450 method, but simplify data interpretation because the elastic properties can be assumed to be
451 constant during shear, and simplifies the analysis described mathematically in Eq. (7).

452 Results revealed that the plastic potential and yield surfaces are different, indicating non-
453 associated flow. Furthermore, the shape of the plastic potential surfaces was qualitatively
454 similar in shape to the Original Cam-clay model surface (Schofield and Wroth, 1968) in that
455 the surfaces were curved, skewed to the left, and had a zero slope near the ultimate value of the
456 q/p' ratio. Many constitutive models for sand, such as Poorooshasb, and Pietruszczak (1985),
457 utilize Drucker-Prager type yield surfaces for which the slope of the yield surface is equal to
458 the stress ratio during yield. The experimental results shown herein, do not support this type of
459 yield surface.

460 The methods described herein constitutes a departure from the manner in which elastoplastic
461 constitutive models are typically calibrated to match experimental data. Typically, basic
462 parameters such as elastic constants and critical state lines are based on measurements, and
463 other modeling constants are adjusted to provide a reasonable match between predictions and
464 triaxial compression experiments. However, it may not be feasible to adjust the modeling
465 constants to match the experimental data if the underlying assumptions about the yield surface
466 shape and flow rule are incorrect. This may result in significant errors when the stress paths
467 imposed in a simulation differ significantly from the stress paths utilized in the experiments.
468 The methods described herein provide a simple and expeditious experimental methodology to
469 measure the yield surface and plastic potential surface slopes, thereby enabling identification

470 of errors in the functional form of elastoplastic constitutive models. The method is particularly
471 useful for the calibration of the isotropic elastoplastic models that are commonly used by
472 designers, and for the assessment and kinematic models developed from bounding surface
473 formulations. We hope that this procedure proves useful for future constitutive model
474 development and refinement.

475 **Acknowledgments**

476 This material is based upon research performed in a renovated collaboratory by the National
477 Science Foundation under Grant No. 0963183, which is an award funded under the American
478 Recovery and Reinvestment Act of 2009 (ARRA). The authors thank Ai Zhong for preparing
479 the Jupyter notebook for data visualization on DesignSafe-CI.

480 **References**

- 481 Al-Tabbaa, A. and Wood, D. M., (1989), "An experimentally based 'bubble' model for clay",
482 Numerical models in geomechanics. NUMOG III. pp. 91-99
- 483 ASCE (2010), "GeoFlorida 2010: Advances in Analyses, Modeling & Design", Geotechnical
484 Special Publication No.199 (GSP199), D.O. Fratta, A.J. Puppala, and B. Muhunthan
485 (editors.), West Palm Beach, FL.
- 486 Baladi G. Y. and Rohani B. (1979), "Elastic-Plastic Model for Saturated Sand," Journal of
487 Geotechnical Engineering, ASCE, 105, p. 465-477.
- 488 Brandenberg, S.J., Kutter, B.L., and Wilson, D.W. (2008). "Fast Stacking and Phase
489 Corrections of Shear Wave Signals in a Noisy Environment.", Journal of Geotechnical
490 and Geoenvironmental Engineering, 134(8), 1154-1165.
- 491 Dafalias, Y. F. (1986), "Bounding surface plasticity. I: mathematical foundation and
492 hypoplasticity," Journal of Engineering Mechanics, ASCE, 112(9), 966-987.

493 Dafalias, Y. F. and Manzari M. T. (2004), "Simple plasticity sand model accounting for fabric
494 change effects", *Journal of Engineering mechanics*, 130(6), 622-634.

495 Eslami, M. (2017). "Experimental Mapping of Elastoplastic Surfaces for Sand and Cyclic
496 Failure of low-Plasticity Fine-grained Soils." Ph.D. Thesis, University of California,
497 Los Angeles, CA

498 Eslami, M.; Brandenburg, S. J.; Zhong, A.; Pradel, D., (2017), "Triaxial Tests on Sand for
499 Yield Surface Mapping", DesignSafe-CI [publisher], Dataset, DOI:
500 <https://doi.org/10.17603/DS23T00>

501 Esteva, M., Brandenburg, S. J., Eslami, M., Adair, A., Kulasekaran, S., (2016), "Modelling
502 Natural Hazards Engineering Data to Cyberinfrastructure." Proceedings of the
503 SciDataCon 2016. 11-13 September 2016, Denver, Colorado. Available at:
504 <http://www.scidatacon.org/2016/sessions/104/paper/282/>

505 Itasca Consulting Group (2011), "Computer Program FLAC 7.0", Minneapolis, MN.
506 www.itascacg.com.

507 Jones, R.M. (2009), "Deformation Theory of Plasticity", Bull Ridge Publishing

508 Kuwano, R., and Jardine, R. J. (2007), "A triaxial investigation of kinematic yielding in
509 sand", *Géotechnique*, 57(7), 563-580.

510 Lade, P. V. (1977), "Elasto-plastic stress-strain theory for cohesionless soil with curved yield
511 surfaces", *Int. Journal of Solids and Structures*, 13(11), 1019-1035.

512 Lade, P. V., and Kim, M. K. (1988), "Single hardening constitutive model for frictional
513 materials II. Yield criterion and plastic work contours", *Computers and*
514 *Geotechnics*, 6(1), 13-29.

515 Masing, G. (1926, September), “Eigenspannungen und verfestigung beim messing”,
516 Proceedings of the 2nd Int. Congress of Applied Mechanics (Vol. 100, 332-5).

517 Menq, F-Y., (2003), “Dynamic properties of sandy and gravelly soils”, Dissertation at the
518 University of Texas, Austin

519 Mróz, Z., Norris, V. A., and Zienkiewicz, O. C. (1979). “Application of an anisotropic
520 hardening model in the analysis of elasto-plastic deformation of soil”,
521 Géotechnique 29, No. 1, 1–34

522 Nawir, H., Tatsuoka, F. and Kuwano, R. (2003), “Viscous effects on the shear yielding
523 characteristics of sand”, *Soils and Foundations*, Vol. 43, No. 6, pp. 33-50

524 Plaxis BV (2015), “Computer Program PLAXIS 2015”, Delft, Netherlands. www.plaxis.nl.

525 Poorooshasb, H. B., (1971), “Deformation of sand in triaxial compression”, Proc., 4th Asian
526 Regional Conf. on SMFE, Bangkok, Vol. 1, pp. 63-66

527 Poorooshasb, H. B., and Pietruszczak, S. (1985), “On yielding and flow of sand; a generalized
528 two-surface model”, *Computers and Geotechnics*, 1(1), 33-58.

529 Poorooshasb, H. B., Holubec, I., and Sherbourne, A. N. (1966) “Yielding and flow of sand in
530 triaxial compression: Part I”, *Canadian Geotechnical Journal*, 3(4), 179-190.

531 Poorooshasb, H. B., Holubec, I., and Sherbourne, A. N. (1967), “Yielding and flow of sand in
532 triaxial compression: Parts II and III”, *Canadian Geotechnical Journal*, 4(4), 376-397.

533 Pradel D., Ishihara K., and Gutierrez M. (1990), “Yielding and Flow of Sand under Principal
534 Stress Axes Rotation”, *Soils and Foundations*, Vol. 30, No. 1, 87-99.

535 Pradel, D., and Lade, P. V. (1990), “Instability and plastic flow of soils. II: Analytical
536 investigation”, *Journal of Engineering Mechanics*, ASCE, 116(11), 2551-2566.

537 Rathje, E., Dawson, C. Padgett, J.E., Pinelli, J.-P., Stanzione, D., Adair, A., Arduino, P.,
538 Brandenberg, S.J., Cockerill, T., Dey, C., Esteva, M., Haan, Jr., F.L., Hanlon, M.,
539 Kareem, A., Lowes, L., Mock, S., and Mosqueda, G. (2017), “DesignSafe: A New
540 Cyberinfrastructure for Natural Hazards Engineering,” ASCE Natural Hazards Review.
541 DOI: 10.1061/(ASCE)NH.1527-6996.0000246

542 Roscoe K. H., and J. B. Burland (1968), “On the Generalised Stress-Strain Behavior of ‘Wet
543 Clay’”, in *Engineering Plasticity*, pp. 535-609. J. Heyman and F. A. Leckie, Eds.
544 Cambridge University Press.

545 Roscoe, K. H. and Schofield, A. N. (1963), “Mechanical Behaviour of an Idealised ‘Wet’
546 Clay”, *Proc. 2nd European Conf. on Soil Mechanics and Foundation Engineering*,
547 Wiesbaden, vol. 1, pp. 47-54

548 Schofield and Wroth (1968), “Critical State Soil Mechanics”, McGraw-Hill.

549 Taiebat, M., and Dafalias, Y. F. (2008), “SANISAND: Simple anisotropic sand plasticity
550 model”, *Int. Journal for Numerical and Analytical Methods in Geomechanics*, 32(8),
551 915-948.

552 Tanimoto, K., and Tanaka, Y. (1986), “Yielding of soil as determined by acoustic
553 emission”, *Soils and Foundations*, 26(3), 69-80. Yasufuku et al, 1991

554 Tatsuoka, F., (2006), “Inelastic Deformation Characteristics of Geomaterial”, *Soil Stress-
555 Strain Behavior: Measurement, Modeling and Analysis*, A collection of papers of the
556 Geotechnical Symposium in Rome, March 16 & 17, 2006, Springer

557 Tatsuoka, F., and Ishihara, K. (1974), “Yielding of sand in triaxial compression”, *Soils and
558 Foundations*, 14(2), 63-76.

559 Tatsuoka, F., and Molenkamp, F. (1983), "Discussion on yield loci for sands", Mechanics of
560 Granular Materials: New Models and Constitutive Relations, Elsevier Science
561 Publisher B.V., pp.75-87.

562 Vermeer, P. A. (1978), "A double hardening model for sand", Geotechnique, 28(4), 413-433.

563 Wood, D. M. (1990) "Soil Behaviour and Critical State Soil Mechanics", Cambridge
564 University Press.

565 Yasufuku, N., Murata, H., and Hyodo, M., (1991), "Yield characteristics of anisotropically
566 consolidated sand under low and high stresses", Soils and Foundations, Vol. 31, No. 1,
567 95-109.

568